International Journal of Robotics and Control Systems
Vol. 5, No. 6, 2025, pp. 3103-3128
ISSN 2775-2658
http://pubs2.ascee.org/index.php/ijrcs

Sine Cosine Algorithm (SCA)-Based on Grid-Connected Doubly Fed Induction Generator (DFIG) Performance Analysis for Shunt Active Power Filter (SAPF)

Ines Lemita [a,1,*], Zoubir Chelli [a,2], Chouaib Souaidia [b,3], Abdallah Lemita [c,4]

[a] Department of Electrical Engineering, Mohamed Cherif Messaadia University, Souk-Ahras, Algeria
[b] ATE Department, Faculty of Technology, Abderrahmane Mira University, Bejaia, Algeria
[c] Department of Electrical Engineering, Echahid Cheikh Larbi Tebessi University, Tebessa, Algeria
[1] i.lemita@univ-soukahras.dz; [2] zoubir.chelli@univ-soukahras.dz; [3] chouaib.souaidia@univ-bejaia.dz;
[4] abdallahlemita@yahoo.fr
* Corresponding Author

ARTICLE INFO

Article history
Received October 04, 2025
Revised December 05, 2025
Accepted December 21, 2025

Keywords
Wind;
Doubly Fed Induction Generator;
Shunt Active Power Filter;
Hysteresis Control;
Model Predictive Current Control;
Sine Cosine Algorithm;
Total Harmonic Distortion

ABSTRACT

Integration of the wind power into the electrical grid to improve grid flexibility with additional generation capacity can also affect the quality of the power, like voltage variations and harmonics. To solve this issue, a grid-side converter has been used like a shunt active power filter (SAPF), mitigating grid current harmonics generated by nonlinear loads while simultaneously managing bidirectional power flow between the grid and the rotor of the doubly fed induction generator (DFIG). The SAPF is controlled using the predictive current control and is supplied by a wind energy system through a DC-link capacitor. This paper presents a modified grid-side converter (GSC) control technique using the sine cosine algorithm (SCA) by tuning the PI regulator's parameters that is designed to keep the constant DC bus voltage and to compensate for system losses. The efficacy of the proposed control approach is modeled and verified according to MATLAB/Simulink, and it offers significant potential for enhancing power quality efficiency, minimizing grid harmonics, and boosting system robustness.

1. Introduction

The environmental impacts, such as the energy disaster, environmental pollution, and low energy efficiency measures, are the serious concerns encountered in world the last decades. To tackle these difficulties and fill the energy needs, the power suppliers have begin shifting to the renewable energy-based power-producing technologies [1].

Due to its high degree of technological maturity, low cost, and zero gas emissions when compared to other renewable sources, the Wind Power Generation System (WPGS) has emerged as one of the most popular renewable energy resources (RER) in recent years. A wind turbine is a mechanical device that uses wind flow to generate rotational energy, which an electrical machine then transforms into electrical energy [2]. The utilization of DFIGs in WPGS has become common. DFIG-based wind turbines offer various benefits over other types. They maximise energy capture over a range of wind

speeds by enabling different speed operation. In order to lower expenses and energy losses, they also employ a partially rated power electronic converter, which usually uses around thirteen percent of the total power output [3], [4]. Wind power depends greatly on wind speed, seasons, location, and many other factors that impede a continuous flow of power to feed loads. Therefore, it is essential to harness the wind's utmost power. Therefore, the MPPT is employed to harvest the maximum power from the wind. Power fluctuation can typically induce voltage and frequency restrictions in weak systems. This can also be a major problem for the system's stability. Hence, there is a requirement for power electronics in wind power systems control to obtain high efficiency and higher performance [5]. Power electronic converters are utilised to match wind turbine characteristics with grid connection specifications, such as frequency, harmonics, active and reactive power, etc. [6].

In general, the stator windings of the DFIG are directly attached to the electrical network, whereas the rotor windings are driven by bidirectional PWM voltage converters (VSC) [7]. Mohd. Hasan Ali [8] described the quality of grid power and DFIG power, which are prime of importance in today's era. But the rapid advancement and great development in the manufacture of electronic components, made the modern power systems capable to contain a combination of linear and nonlinear loads. Recently, the extensive utilization of power electronic components (transistors, thyristors, etc.) as switching devices in power converters (such as diode or thyristor rectifiers) has significantly expanded. Consequently, harmonics continue to be produced by nonlinear loads, which compel the power system to function at a low power factor, diminished efficiency, distorted current and voltage waveforms, and heightened losses in transmission and distribution lines [9]. Passive filters have historically been used to solve problem with power quality. Unfortunately, passive filters are heavy and can only filter the particular frequencies for which they are tuned. An inventive method for enhancing electrical network power quality is the shunt active power filter (SAPF). SAPF's tiny size, versatility, and superior filtering capabilities are some of its benefits.

Generally, the SAPF is a three-phase current-controlled voltage source inverter with a DC-side storage capacitor and AC-side interfacing filter inductors. It serves as a current source supplying the load with proper harmonic currents and reactive power to maintain balanced three-phase supply currents with pure sinusoidal [10], [11].

The creation of reference currents and the current control are the main operation of the SAPF. For reference current extraction [12], synchronous reference frame, capacitor voltage control, neural networks, Fourier series, Kalman filter [13], and pq theory [14], a number of techniques have been developed. Synchronous reference frame (SRF) theory with direct power control (DPC) [9].

The predominant contemporary tracking methodologies are hysteresis and linear pulse width modulation (PWM). Hysteresis is a nonlinear control method in which the current error is regulated using a hysteresis band controller. Switching signals are altered when a current error exceeds a specific threshold [15]. A tight hysteresis band is necessary to ensure precise current tracking, leading to a high switching frequency. PWM is a linear control methodology that employs a proportional-integral (PI) controller to produce reference voltage signals. A modulating stage is necessary, utilizing either carrier triangular waveforms or space vector modulation (SVM), to produce the requisite gating signals. Nonetheless, PI control in the stationary reference frame yields inadequate and sluggish responses with subpar tracking performance due to the extensive frequency spectrum of the harmonic content [16].

Due to these flaws in traditional control approaches, it has been discovered that there is a need for a simple and precise current tracking ability methodology. In this paper, an MPCC algorithm is employed in SAPF due to its high accuracy, simple idea, and easy addition of system nonlinearities [17], [18].

In addition, DC interface voltage of the VSI is controlled by using a classical PI controller. In classical technique the derived PI values are not agreeable. Thus, by applying the SCA control program, the derivedPI values are exact and maintain the constant DC bus voltage when its compared with the classical PI controller.

Generally, in this work, two different control mechanisms are taken up for implementation. In order to balance current harmonics and reactive power, the Hysteresis control and the MPC algorithm are utilized to control the SAPF power switches to produce the opposite harmonics and to inject them at the point of common coupling (PCC). The second technique gave by far the best outcomes. In addition, the DC interface voltage of the VSI is adjusted by utilising the SCA-PI control approach, verified by a simulation with MATLAB software.

2. System Description

Fig. 1 shows the basic block diagram of a grid-connected Doubly Fed Induction Generator (DFIG)-based Wind Power Generation System (WPGS). The system includes a wind turbine, gearbox, a DFIG, back-to-back converters, and a bridge rectifier acting as a nonlinear load. The DFIG stator is directly connected to the grid, and the rotor is connected via back-to-back converters. The nonlinear load introduces current harmonics at the point of common coupling, which are mitigated using a shunt active power filter (SAPF). The SAPF consists of: three-leg voltage source inverter (VSI) with a DC-link capacitor and six IGBT switches with anti-parallel diodes. Its effectiveness depends on generating a reference signal that mirrors the load harmonics. In this work, the instantaneous active and reactive power (p–q) method is used to extract the reference harmonics. Predictive current control (MPCC) manages the SAPF switching, while the SCA-PI controller maintains the DC-link voltage under varying disturbances. The generated compensating currents are injected at the PCC to cancel the harmonics. The performance of the SAPF and its control strategies was validated through MATLAB simulations.

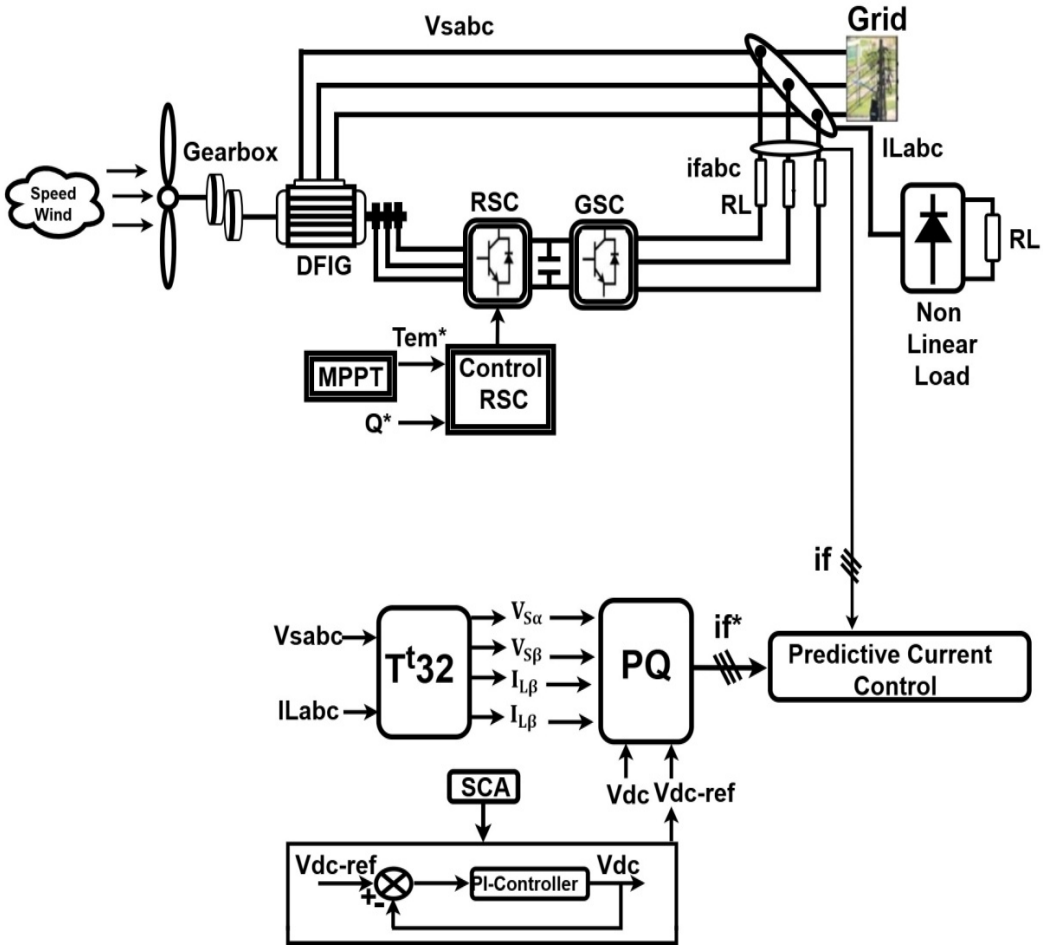

Fig. 1. Principle scheme of an SAPF fed by a wind system

3. Wind Power Generation System (WPGS)

Generally, wind turbine system involves two fundamental subsystems: mechanical and electrical. The aerodynamic turbine and DFIG are connected via a gearbox (Fig. 2). The **WPGS** converts the wind's kinetic energy $\mathbf{P_w}$ into mechanical power $\mathbf{P_m}$, which is transformed into electrical power $\mathbf{P_e}$. The generated electrical power is fed directly into the grid through power converters.

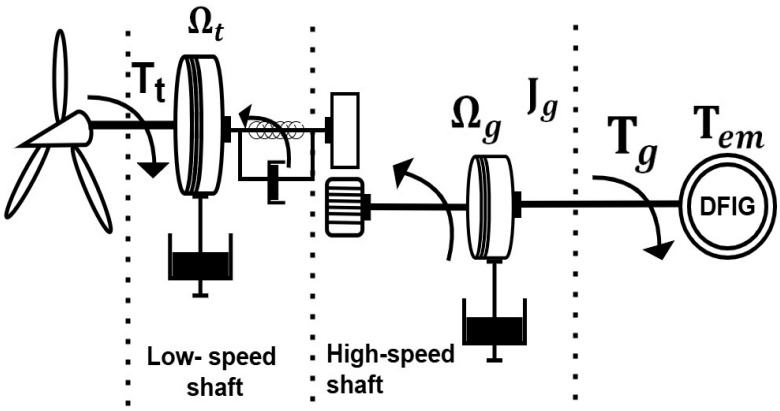

Fig. 2. Mechanical parts-based DFIG [19]

3.1. Modeling of the Wind Turbine

The mechanical power generated by the wind turbine (Fig. 3) is expressed by [19]:

$$P_m = \frac{1}{2}\rho A C_p(\lambda,\beta)V^3 \tag{1}$$

Where V is the wind speed (in $m.s^{-1}$), A is the swept area (m^2), C_p is the turbine's performance coefficient which depends on the rotor blades' pitch angle of β (in degrees), and ρ is the air density ($kg.m^{-3}$).

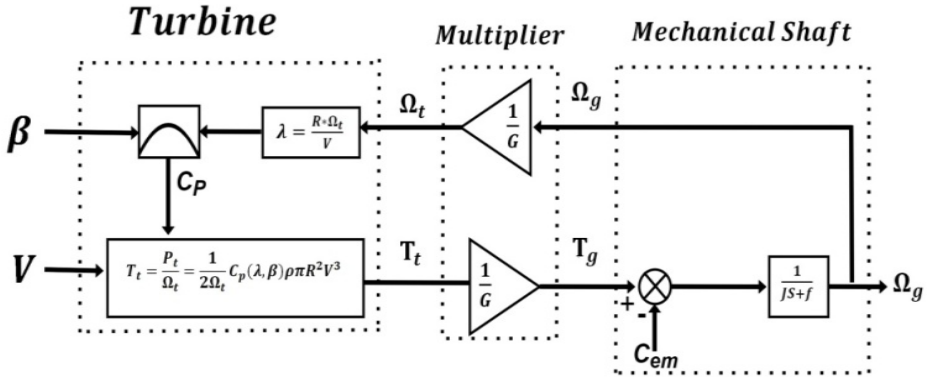

Fig. 3. Block diagram of wind turbine [21]

The tip-speed ratio is λ. The ratio (λ) is given by:

$$\lambda = \frac{R\Omega_t}{V} \tag{2}$$

Here R denotes the blade length (in $meters$). The turbine rotor's the rotational speed is presented by Ω_t (in $rad.s^{-1}$). The power coefficient of $C_p(\lambda,\beta)$ is provided from the following expression:

$$C_p(\lambda,\beta) = 0.5176\left[\left(\frac{116}{\lambda_i} - 0.4\beta - 5\right)\frac{e^{-21}}{\lambda_i} + 0.0068\lambda\right] \tag{3}$$

$$\frac{1}{\lambda_i} = \frac{1}{\lambda + 0.08} - \frac{0.035}{\beta^3 + 1} \tag{4}$$

The mechanical torque of turbine is given by the division of turbine power and speed rotation as detailed in following function:

$$T_t = \frac{P_t}{\Omega_t} = \frac{1}{2\Omega_t} C_p(\lambda, \beta) \rho \pi R^2 V^3 \tag{5}$$

In this context, ρ denotes the density's air, R is the turbine radius, V is the wind velocity, λ is the tip-speed ratio, Ω_t represents the turbine's mechanical angular velocity.

3.2. Multiplier Model

The small speed of the turbine is transferred to maximum speed via a gearbox to be able to turn the DFIG shaft [20]. The equation expressing the mechanical coupling between the turbine and DFIG is given in the following function:

$$\begin{cases} \Omega_t = \dfrac{\Omega_g}{G} \\ T_g = \dfrac{T_t}{G} \end{cases} \tag{6}$$

Where $\boldsymbol{T_g}$ Is the electromagnetic torque of DFIG and $\boldsymbol{G}$ is the gear ratio.

3.3. Mechanical Equation of the Shaft

The mechanical equation of the rotating parts is detailed in (7) [21]:

$$J \frac{d\Omega_m}{dt} = T_t - T_{em} - f\Omega_g \tag{7}$$

Where $\boldsymbol{J}$ is the system total inertia, $\boldsymbol{f}$ is the coefficient of viscous fraction.

3.4. Maximum Power Point Tracking (MPPT)

Fig. 4 illustrates the theory of MPPT control for a wind turbine without regulating the rotational speed. The purpose is to enhance the capture of wind energy by monitoring the ideal torque. $\boldsymbol{T^*_{em}}$ [22]–[25]:

$$T^*_{em} = K\Omega^2_m \tag{8}$$

With

$$K = \frac{1}{2}\pi\rho R^5 \frac{C_{pmax}}{\lambda^3_{opt}} \tag{9}$$

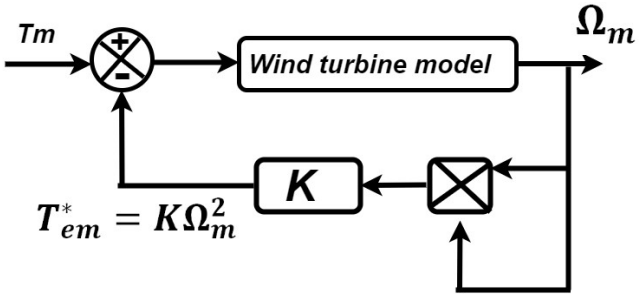

Fig. 4. MPPT control strategy [21]

3.5. Dynamic Model of a DFIG

The electrical expressions in the (d, q) reference can be written by the following differential equations [26], [27]:

$$\begin{cases} V_{ds} = R_s I_{ds} + \dfrac{d\Phi_{ds}}{dt} - \omega_s \Phi_{qs} \\ V_{qs} = R_s I_{qs} + \dfrac{d\Phi_{qs}}{dt} + \omega_s \Phi_{ds} \\ V_{dr} = R_r I_{dr} + \dfrac{d\Phi_{dr}}{dt} - (\omega_s - \omega)\Phi_{qr} \\ V_{qr} = R_r I_{qr} + \dfrac{d\Phi_{qr}}{dt} + (\omega_s - \omega)\Phi_{dr} \end{cases} \tag{10}$$

Where R_s and R_r denote the stator and rotor's respective phase resistances.

In the (d, q) reference frame, the stator and rotor fluxes formulas are [28]:

$$\begin{cases} \Phi_{sd} = L_s I_{sd} + M I_{rd} \\ \Phi_{sq} = L_s I_{sq} + M I_{rq} \\ \Phi_{rd} = L_r I_{rd} + M I_{rd} \\ \Phi_{rq} = L_r I_{rq} + L I_{rq} \end{cases} \tag{11}$$

Where L_s and L_r denoted the inductances of the stator and rotor, while M is the mutual inductance linking both windings. In addition, I_{sd}, I_{sq},I_{rd}, and I_{rq}refer to the d- and q-axis components of the stator and rotor currents [29]–[31].

The DFIG electromagnetic torque formula is:

$$T_{em} = \frac{PM}{L_s}\left(\Phi_{sq} I_{rd} - \Phi_{sd} I_{rq}\right) \tag{12}$$

The following equation expressed how state-space equations in the synchronous reference frame, with the d-axis aligned along the stator flow, can be used to define the DFIG model [32]:

$$\begin{cases} V_{ds} = 0 \\ V_{qr} = V_s = \omega_s \Phi_{ds} \end{cases} \tag{13}$$

The stator's active and reactive powers provided to the grid, are given as follows [33], [34]:

$$\begin{cases} P_s = V_{ds} I_{ds} + V_{qs} I_{qs} \\ Q_s = V_{qs} I_{ds} - V_{ds} I_{qs} \end{cases} \tag{14}$$

The expressions of rotor voltages as a function of rotor currents [35]:

$$\begin{cases} V_{dr} = R_r I_{dr} + \sigma L_r \dfrac{dI_{dr}}{dt} - g\omega_s \sigma L_r I_{qr} \\ V_{qr} = R_r I_{qr} + \sigma L_r \dfrac{dI_{qr}}{dt} + g\omega_s \sigma L_r I_{dr} + g\dfrac{MV_s}{L_s} \end{cases} \tag{15}$$

Where the DFIG's dispersion coefficient is defined by [36]:

$$\sigma = \left(1 - \frac{M^2}{L_s L_r}\right) \tag{16}$$

4. Shunt Active Power Filter (SAPF)

The shunt active power filter (SAPF) is a power electronic device that is mainly used to eliminate currents harmonics produced by nonlinear load, compensate reactive power and improve power factor by generating or absorbing reactive currents. The SAPF injects the equal and opposite harmonic current for making the grid current sinusoidal [37].

4.1. PQ Theory Algorithm

The initial step of the SAPF process involves the creation of reference current. The predominant method for generating reference current generated from the instantaneous active and reactive power approach (p-q theory), as depicted in Fig. 5, proposed by Akagi in 1983, which considers the three-phase system as a unified system.

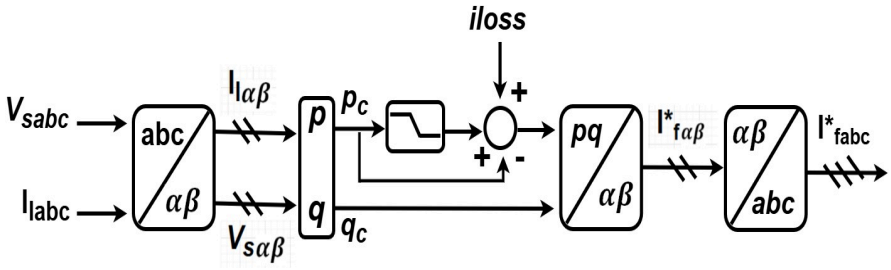

Fig. 5. Block diagram of PQ theory [38]

The PQ algorithm is based on a set of instantaneous power, where three-phase supply voltages (V_{sa}, V_{sb}, V_{sc}) and currents load (I_{la}, I_{lb}, I_{lc}) are converted by the Clarke transformation (α-β) [38], [39], and written as:

$$\begin{bmatrix} x_\alpha \\ x_\beta \end{bmatrix} = \sqrt{\frac{2}{3}} \begin{bmatrix} 1 & -\frac{1}{2} & -\frac{1}{2} \\ 0 & \frac{1}{2\sqrt{3}} & -\frac{1}{2\sqrt{3}} \end{bmatrix} \begin{bmatrix} x_a \\ x_b \\ x_c \end{bmatrix} \tag{17}$$

Where x stands for voltage and current. Invariant power transformation uses factor 2/3.

$$\begin{bmatrix} V_{s\alpha} \\ V_{s\beta} \end{bmatrix} = \sqrt{\frac{2}{3}} \begin{bmatrix} 1 & -\frac{1}{2} & -\frac{1}{2} \\ 0 & \frac{1}{2\sqrt{3}} & -\frac{1}{2\sqrt{3}} \end{bmatrix} \begin{bmatrix} V_{sa} \\ V_{sb} \\ V_{sc} \end{bmatrix} \tag{18}$$

$$\begin{bmatrix} I_{l\alpha} \\ I_{l\beta} \end{bmatrix} = \sqrt{\frac{2}{3}} \begin{bmatrix} 1 & -\frac{1}{2} & -\frac{1}{2} \\ 0 & \frac{1}{2\sqrt{3}} & -\frac{1}{2\sqrt{3}} \end{bmatrix} \begin{bmatrix} I_{la} \\ I_{lb} \\ I_{lc} \end{bmatrix} \tag{19}$$

Following the conversion of voltages and currents, the instantaneous values of real power $\boldsymbol{p}$, and imaginary power $\boldsymbol{q}$, are:

$$\begin{bmatrix} \mathrm{p} \\ \mathrm{q} \end{bmatrix} = \begin{bmatrix} \mathrm{V_{s\alpha}} & \mathrm{V_{s\beta}} \\ -\mathrm{V_{s\beta}} & \mathrm{V_{s\alpha}} \end{bmatrix} \begin{bmatrix} \mathrm{I_{l\alpha}} \\ \mathrm{I_{l\beta}} \end{bmatrix} \tag{20}$$

The (α-β) axis currents references are provided as:

$$\begin{bmatrix} I^*_{f\alpha} \\ I^*_{f\beta} \end{bmatrix} = \frac{1}{V^2_{s\alpha} + V^2_{s\beta}} \begin{bmatrix} V_{s\alpha} & -V_{s\beta} \\ V_{s\beta} & V_{s\alpha} \end{bmatrix} \begin{bmatrix} \tilde{p} \\ \mathrm{q} \end{bmatrix} \tag{21}$$

By using the inverse Clarke transformation on the stationary-frames reference currents, the three-phase reference current of SAPF is determined:

$$\begin{bmatrix} I_{fa}^{*} \\ I_{fb}^{*} \\ I_{fc}^{*} \end{bmatrix} = \sqrt{\frac{2}{3}} \begin{bmatrix} 1 & 0 \\ -\frac{1}{2} & \frac{1}{2\sqrt{3}} \\ -\frac{1}{2} & -\frac{1}{2\sqrt{3}} \end{bmatrix} \begin{bmatrix} I_{f\alpha}^{*} \\ I_{f\beta}^{*} \end{bmatrix} \quad (22)$$

4.2. Conventional Hysteresis Current Control Technique (HCC)

Feedback-based current control techniques are used in high-current control (HCC) technology. PWM signals for the converters are generated by HCC according to the hysteresis band restrictions. As shown in Fig. 6, the reference signal from the control circuit is compared with the source current. When the current reaches the upper boundary of the hysteresis band, the upper switch is deactivated and the lower switch is turned on, causing the current to drop. Conversely, when the current falls below the lower threshold, the lower switch is turned off and the higher switch is triggered, pushing the current to rise [40], [41].

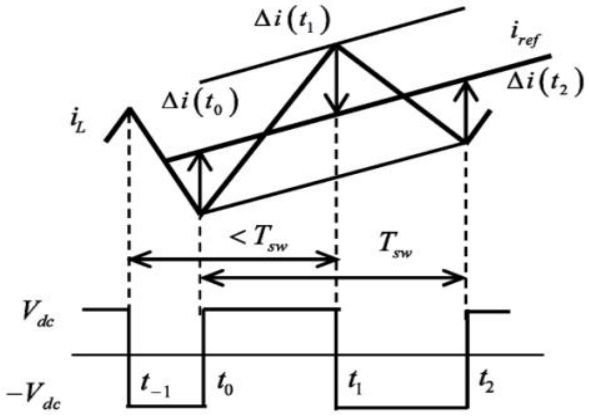

Fig. 6. Hysteresis current control PWM controller [38]

Some advantages and disadvantages of this technology are listed below:

A few advantages:

- the easiness of implementation.
- the good dynamics and robustness.

A few disadvantages:

- the switching frequency is variable, and it varies according to the width of the hysteresis band and the current's rate of change.
- the action control is applied separately for each of the three phases.
- the electrotechnical system structure enforces that at any instant the sum of the three [42].

5. Predictive Current Control

The foundation of the Model Predictive Control (MPCC), as illustrated in Fig. 7, lies in forecasting the behavior of controlled variables using the system's model. The controller will utilize this information to implement the optimal voltage vector from the eight available options. A selection criterion must be established. This criterion comprises a cost function that will be assessed for the

anticipated values of the variables to be regulated. Will be selected and sent to the filter switches [43], [44].

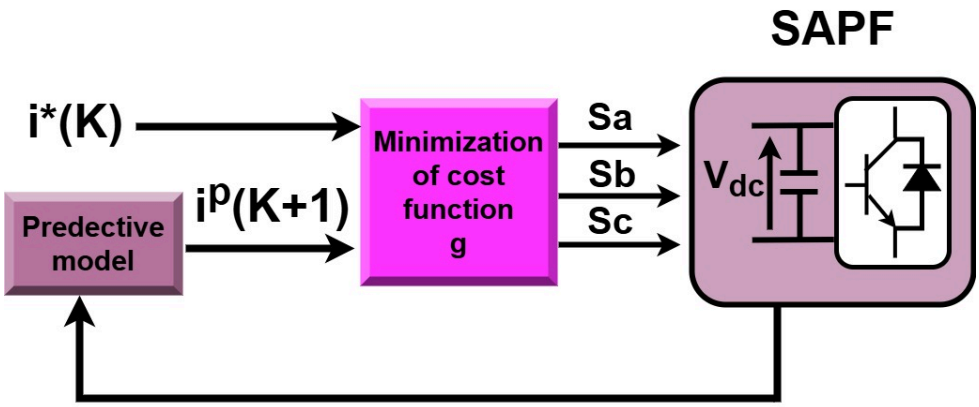

Fig. 7. Predictive current control block diagram [43]

This MPCC technique applied in this work be summarized through the steps:

- Extrapolating reference current;
- Calculate predicted SAPF currents;
- Build the converter model and its possible switching sequences (voltage vectors); and
- Define an appropriate cost function g.

1. Extrapolating the reference current (given in (22)) by using Lagrange method defined by:

$$i_{fx}^{*}(k+1) = 3i_{fx}^{*}(k) - 3i_{fx}^{*}(k-1) + i_{fx}^{*}(k-2) \tag{23}$$

2. The predicted currents of the SAPF at the discrete time step (k + 1) are given by:

   The one phase equivalent circuit of the system composed of SAPF + grid + nonlinear load is shown in Fig. 8.

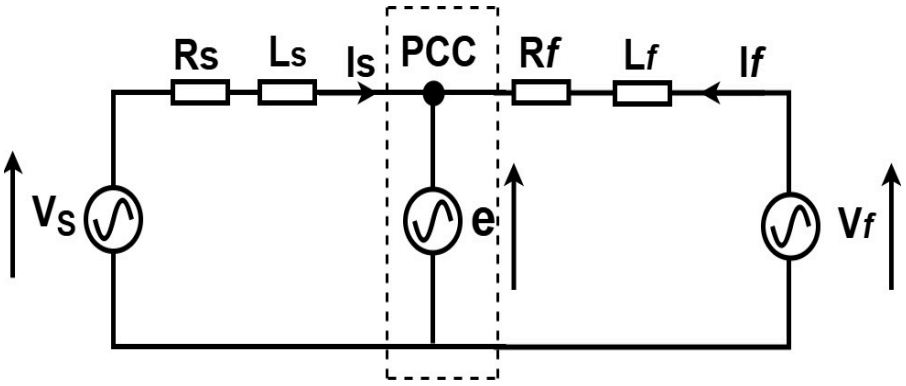

Fig. 8. One phase equivalent circuit of an SAPF connected to a nonlinear load fed by the grid [43]

$$\frac{di_f}{dt} + \frac{R_f}{L_f} i_f = \frac{e - V_f}{L_f}$$

$$i_{fx}^{p}(K+1) = Ai_{fx}(K) + B\left(V_s(K) - V_f(K)\right) \tag{24}$$

$$A = e^{-T_s\left(R_f/L_f\right)} \approx 1 - \frac{R_f}{L_f}T_s \tag{25}$$

$$B = \frac{1 - e^{-\left(T_s/\tau\right)}}{R_f} \approx \frac{1 - 1\left(\frac{R_f}{L_f}T_s\right)}{R_f} \approx \frac{T_s}{L_s} \tag{26}$$

Where $\boldsymbol{x}$ represents phase (**a**, **b** and **c**), e represents the mains phase voltage at the Point of Common Connection, T_s is the sampling period, i_f denotes the corresponding phase current supplied by the SAPF, $V_f$is the average voltage of the SAPF leg. The filter inductors are characterized by their resistance $R_f$and inductance L_f.

Here the coefficients A, $B$are approached by a Taylor series. The time constant τ of the stage's output of SAPF is denoted as $\tau = L_f/R_f$.

$$(K+1) = \left(1 - \frac{R_f}{L_f}T_s\right) i_{fx}(K) + \frac{T_s}{L_s}\left(V_s(K) - V_f(K)\right) \tag{27}$$

3. The voltage vector (Fig. 9) which minimizes the current error is selected and the related optimal switching state signals are provided to the filter switches using Table 1. The DC source, the switching state of the power switches *Sx*, for $x = \overline{1,6}$, can be given by *Sa*, *Sb*, and *Sc*.

$$S_a = \begin{cases} 1 & if S_1 \ on and \ S_4 \ off \\ 0 & if S_1 \ on and \ S_4 \ on \end{cases} \tag{28}$$

$$S_b = \begin{cases} 1 & if S_2 \ on and \ S_5 \ off \\ 0 & if S_2 \ on and \ S_5 \ on \end{cases} \tag{29}$$

$$S_c = \begin{cases} 1 & if S_3 \ on and \ S_6 \ off \\ 0 & if S_3 \ on and \ S_6 \ on \end{cases} \tag{30}$$

These switching signals introduce the value of the voltages' output

$$V_a = S_a V_{dc} \tag{31}$$

$$V_b = S_b V_{dc} \tag{32}$$

$$V_a = S_c V_{dc} \tag{33}$$

Where V_{dc} is the DC source voltage.

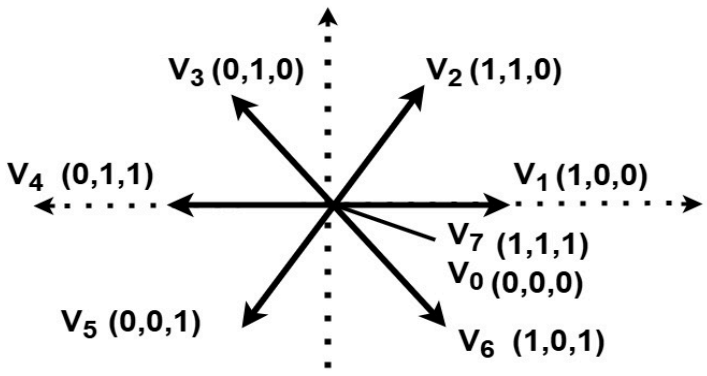

Fig. 9. Voltage vectors in the complex plane [45]

Table 1. Switching states and voltage vectors

S_a	S_b	S_c	Voltage vector V
0	0	0	$V_0 = 0$
1	0	0	$V_1 = \frac{2}{3}V_{dc}$
1	1	0	$V_2 = \frac{1}{3}V_{dc} + j\frac{\sqrt{3}}{3}V_{dc}$
0	1	0	$V_3 = -\frac{1}{3}V_{dc} + j\frac{\sqrt{3}}{3}V_{dc}$
0	1	1	$V_4 = -\frac{2}{3}V_{dc}$
0	0	1	$V_5 = -\frac{1}{3}V_{dc} - j\frac{\sqrt{3}}{3}V_{dc}$
1	0	1	$V_6 = \frac{1}{3}V_{dc} - j\frac{\sqrt{3}}{3}V_{dc}$
1	1	1	$V_7 = 0$

4. Cost function g evaluates the error between the generated reference current and the predicted current calculated by the prediction law in the next sampling time for the all eight possible voltage vectors.

$$g = \left|i_{f\alpha}^{*}(k+1) - i_{f\alpha}^{p}(k+1)\right| + \left|i_{f\beta}^{*}(k+1) - i_{f\beta}^{p}(k+1)\right| \quad (34)$$

Where $i_{f\alpha}^{*}(k+1)$, $i_{f\alpha}^{p}(k+1)$, and $i_{f\beta}^{*}(k+1)$, $i_{f\beta}^{p}(k+1)$ are the real and imaginary parts of refer components of the predicted and reference filter currents in the stationary frame, respectively [45], [46].

6. Voltage Regulation of DC Link

The quality and the SAPF performance depend strongly on the accuracy of the compensating reference current, in which the dc link voltage control plays a significant role. Variations in the compensating current can cause decrease or increase of dc-link voltage (Vdc). To guarantee that the VSI operates correctly at a given reference value, the inverter's DC side must remain stable. For this purpose, both controllers have been compared and incorporated into the system [47]:

- PI controller
- SCA-PI controller

6.1. PI Controller

A conventional approach is employed for controlling the DC-link voltage, where a PI controller with appropriately chosen proportional and integral gains, is used, as depicted in Fig. 10. This controller minimizes voltage fluctuations and ensures a stable DC-link voltage response. In this study, the PI gains are determined using a traditional pole placement method [48], [49].

$$\frac{V_{dc}(S)}{V_{dc}^{*}(S)} = \frac{K_P.S + K_i}{C.S^2 + K_P.S + K_i} = \frac{\frac{K_P}{K_i}.S + 1}{\frac{C}{K_i}.S^2 + \frac{K_P}{K_i}.S + 1} \quad (35)$$

$$F(S) = \frac{1}{\frac{1}{\omega_n^2}.S^2 + \frac{2\xi}{\omega_n}.S + 1} \quad (36)$$

$$K_P = 2.\xi.\omega_n.C \quad (37)$$

$$K_i = C.\omega_n^2 \tag{38}$$

Where C, n and ξ are DC-link capacitor, damping factor and natural frequency.

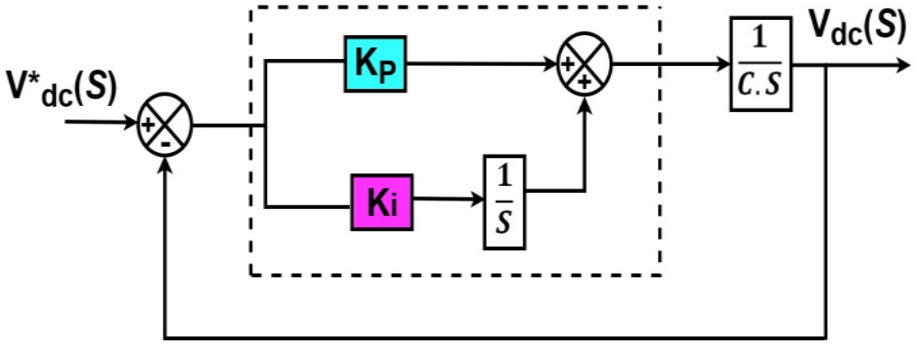

Fig. 10. PI controller of DC-link voltage [49]

6.2. SCA-PI controller

Fig. 11 illustrates the proposed SCA-PI controller. The DC link capacitor voltage is regulated to match reference voltage. The resulting error is processed by SCA-PI controller. In order to keep the DC-link voltage level constant, the SCA-PI controller's output is added to the fundamental active component of the compensating current. This resultant reference current is then compared using hysteresis band and predictive current control with the measured compensating filter current, producing an error signal. This error signal determines the switching actions of VSI [50], [51].

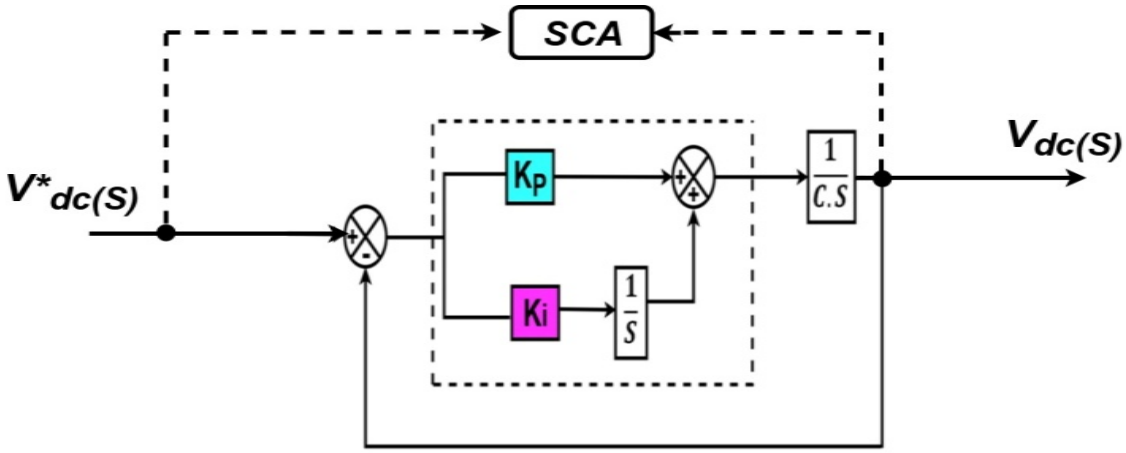

Fig. 11. SCA-PI controller of DC-link voltage control [49]

7. Sine Cosine Algorithm (SCA)

To attain an optimal regulation of the DC-link voltage, in this paper, the Sine Cosine Algorithm (SCA) has been employed to tune PI parameters Kp and Ki. The SCA was selected due to its simplicity, fast convergence, and strong ability to escape local minima. In this study, the SCA algorithm (Fig. 12) iteratively adjusts the PI parameters to minimize the voltage error between the reference Vdc and the measured value. The objective (cost) function is chosen based on the dynamic performance of the DC-link voltage response, taking into consideration criteria such as settling time, rise time, overshoot and steady-state error. Through successive update equations driven by sine and cosine operators, the SCA explores the search space and identifies the optimal PI gains that yield the most stable and rapid Vdc regulation. The optimized controller significantly improves the system's transient response and ensures a robust DC-link voltage under different load variations.

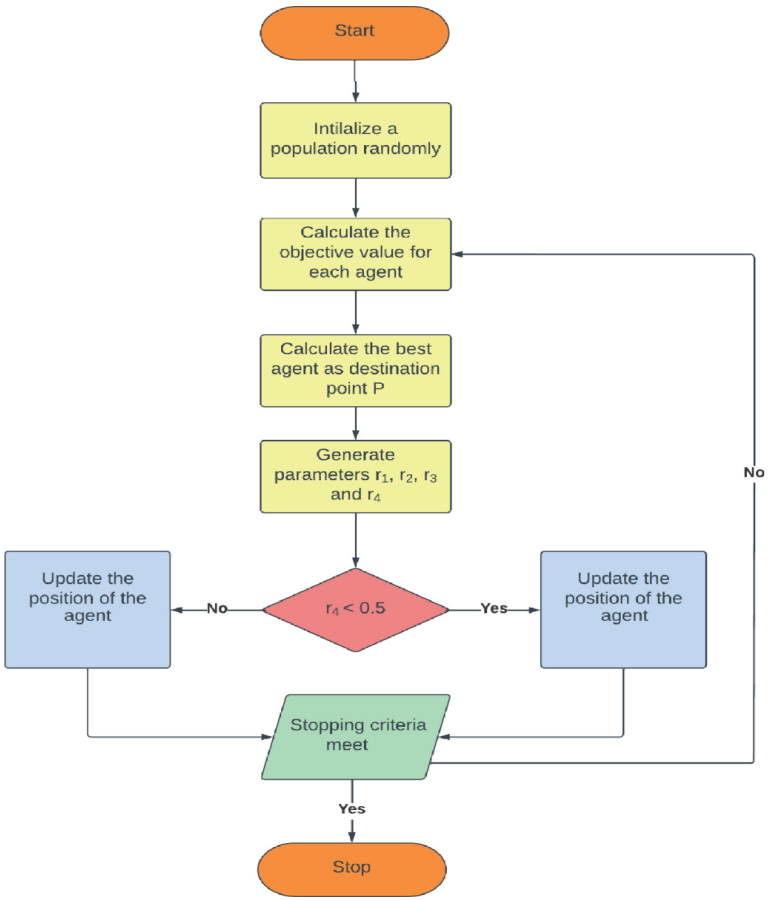

Fig. 12. Flowchart of SCA algorithm [55]

SCA is relatively an efficient new algorithm in the field of metaheuristic, which is visualized from sine and cosine function trends [52], [53]. The periodicity of sine and cosine within [−1, 1] enhances the algorithm's exploitation ability. The optimisation of this approach occurs in two phases:

- During the exploration phase, an optimisation algorithm generates a promising region by rapidly using random solutions from the solution set.
- During the exploitation phase, the alteration of random solutions and variations occurs gradually, leading to the attainment of global optima.

The sine-cosine algorithm is mathematically described by the position-updating equations for the two phases [54]:

$$X_j^{t+1} = X_j^t + r_1 \times sin(r_2) \times \left| r_3 P_j^t - X_j^t \right| \tag{39}$$

$$X_j^{t+1} = X_j^t + r_1 \times cos(r_2) \times \left| r_3 P_j^t - X_{jj}^t \right| \tag{40}$$

In generally (39) and (40) can be combined as one equation as follows in (41).

$$X_j^{t+1} = \begin{cases} X_j^t + r_1 \times sin(r_2) \times \left| r_3 P_j^t - X_j^t \right|, & r_4 < 0.5 \\ X_j^t + r_1 \times cos(r_2) \times \left| r_3 P_j^t - X_{jj}^t \right|, & r_4 \geq 0.5 \end{cases} \tag{41}$$

Where, the variables, $\boldsymbol{X_j^t}$ and $\boldsymbol{X_j^{t+1}}$ represent the $\boldsymbol{i^{th}}$ location of the current solution during iteration $\mathbf{t}$ and the next iteration $\boldsymbol{t+1}$, respectively. The $\boldsymbol{r_1}$, $\boldsymbol{r_2}$, $\boldsymbol{r_3}$ and $\boldsymbol{r_4}$ denote randomly generated integers, whereas $\boldsymbol{P_j^t}$ refers to the most optimal solution at the $\boldsymbol{i^{th}}$ position in the collection of solutions [55], [56].

According to the provided equations, SCA (Fig. 13) is distinguished by the following four parameters: r_1, r_2, r_3, and r_4. The parameter r_1 defines the potential area where the solution and the target can be positioned, potentially within a defined zone. This parameter enables for the investigation and utilisation of a search area while keeping an appropriate balance between them. The technique divides the maximum iteration count in half, devoting one half to diversification and the other half to increasing exploration within a suitable search area. The parameter r_2 defines the orientation of the moment for a particular solution. The parameter r_3 quantifies the relevance of the weight provided to P_j^t. r_4 defines equal switching from sine to cosine or vice versa within range of [0, 1] [57], [58].

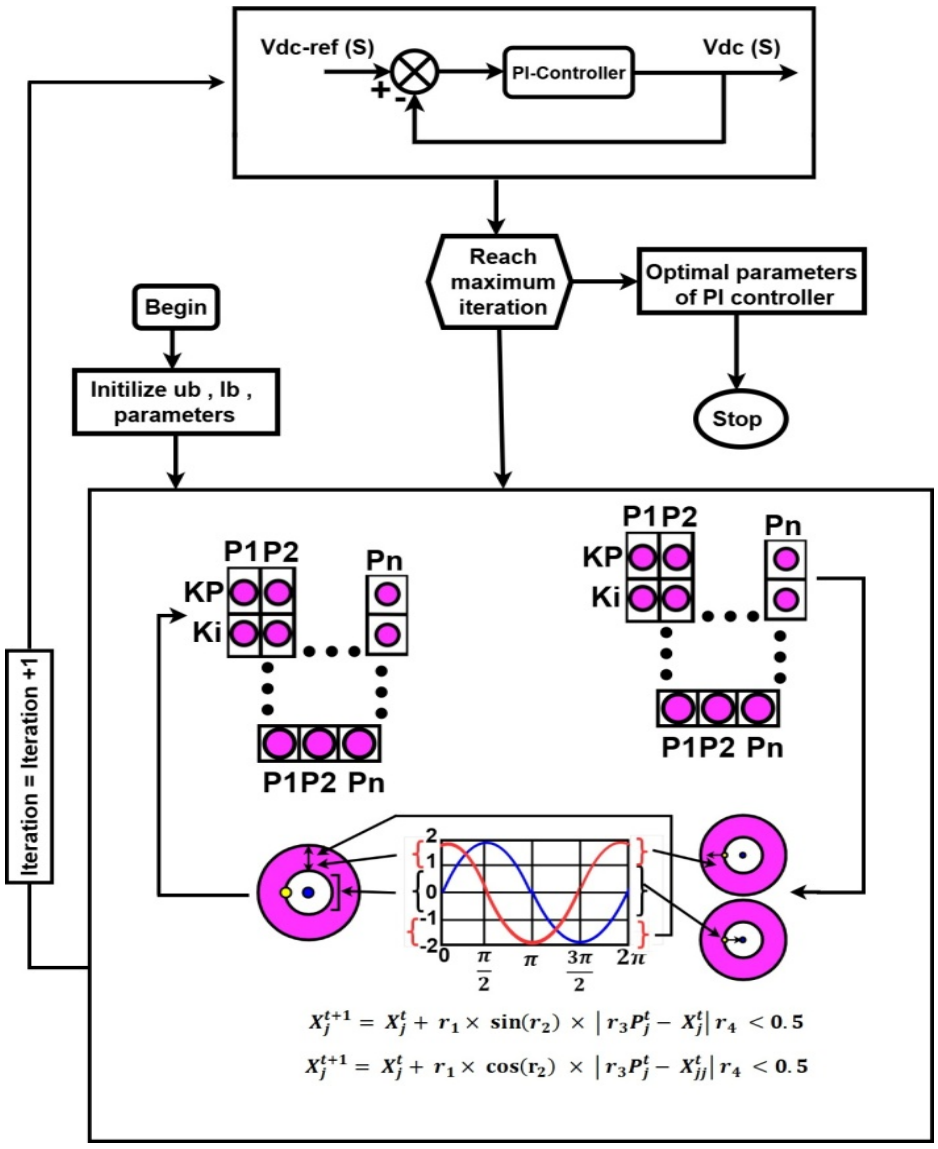

Fig. 13. SCA implementation block diagram

The mathematical updates for r_1 , r_2 , r_3 and r_4 are as following:

$$\begin{cases} r_1 = a - a \times \dfrac{t}{T} \\ r_2 = (2 \times \pi) \times rand \\ r_3 = 2 \times rand \\ r_4 = rand \end{cases} \tag{42}$$

Where T is the highest iteration, t is the present iteration, and a is a constant.

Fig. 14 shows the movement of populations (or search agents) around the best solution. Equation (41) defines a distance between two solutions in the search space. By adjusting the amplitude of sine-cosine functions, the solutions can move beyond the region between their respective targets, ensuring effective exploration of the search space. Conversely, the periodic nature of sine-cosine functions promotes exploitation by allowing a solution to shift closer to another. This behaviour is illustrated in the Fig. 15 [59], [60].

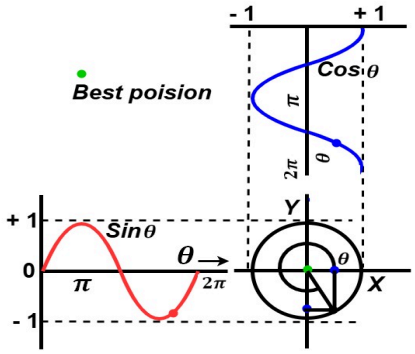

Fig. 14. Movement of populations around the best solution [57]

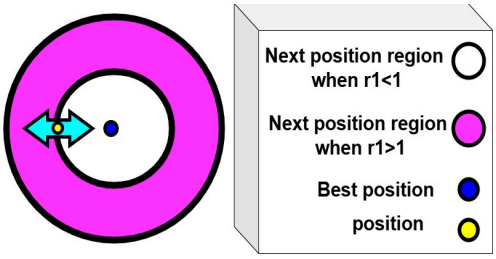

Fig. 15. Movement of the new populations based on r_1 [60]

8. Results and Discussions

The simulations created in this study (Fig. 1) are executed using MATLAB Sim Power System. The simulation shows clearly the efficacy of the active filter in eliminating current harmonics caused by nonlinear load. Furthermore, it demonstrates the infusion of electric power derived from the wind system into the PCC. The harmonics affect not just the source but also additional loads connected to that source. The sampling duration employed in simulation tests is 0.2 seconds. The global system is modeled using two control methods: Hysteresis Control and predictive control of the active shunt filter (inverter) for harmonic compensation and reactive power management. The results of the DC-link voltage loop with the PI and SCA-PI controllers are also analyzed. The system begins without harmonics compensation and SAPF is turned on at 0.05 sec.

Two control methods have been studied in this works for harmonic compensation and reactive power management; hysteresis control and predictive control. The results of the DC-link voltage loop with PI and SCA-PI are also analysed. The performance of SAPF is investigated for the following circumstances:

- System without SAPF.
- System with hysteresis control strategy for the SAPF and PI Controller.
- System with predictive control strategy for the SAPF and PI Controller.
- System with predictive control strategy for the SAPF and (SCA-PI Controller).
- Comparison of DC-link voltage (PI and SCA-PI controller).

8.1. Case I: System without Shunt Active Power Filter

Without a SAPF, the nonlinear load (rectifier) injects harmonics (3rd, 5th, 7th, etc.), which creates several disturbances in the electrical network among them:

- Distorted currents illustrated in Fig. 16 and Fig. 17. The source currents are equivalent to those of the nonlinear load (Is = Il = 2.91 A), characterized by a spectrum comprising solely odd-order harmonics (excluding multiples of three) and a THDi of 26.24% (Fig. 18). These distorted currents increase heating in transformers/cables, reduced efficiency and higher I²R losses.
- Distorted voltage: the harmonic currents flowing through network impedance distort the supply voltage, shorten equipment lifetime and reduce power quality.
- Poor power factor: the reactive power plus harmonics content reduce the power factor.

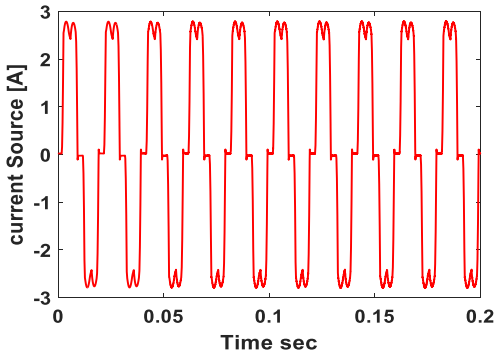

Fig. 16. Current load

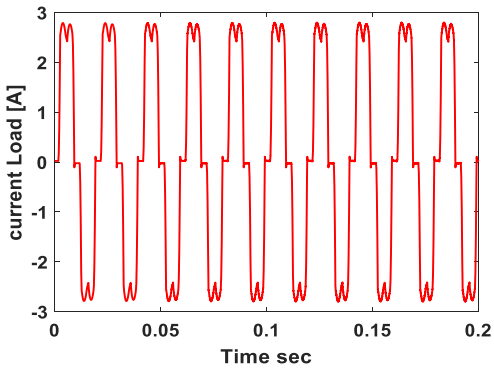

Fig. 17. Source current

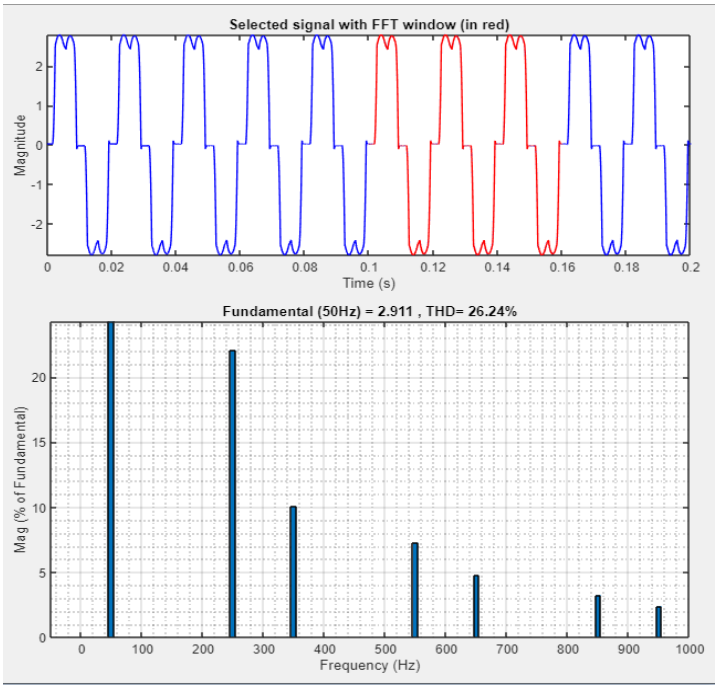

Fig. 18. Spectral analysis of the source current before commissioning of the SAPF

8.2. Case II: The System with Hysteresis Control Strategy for the SAPF and PI Controller

In order to eliminate harmonics currents, compensate reactive power and ameliorate power factor, adding a SAPF is crucial. The SAPF generates a reference current obtained from a harmonic detection using p-q method. The inverter's output current is forced to remain inside a hysteresis band

around the reference current. This makes the inverter produce a voltage that pulls the current back inside the band.

The PI controller is utilized to adjust the SAPF so that the DC-link capacitor voltage stays constant. The PI output generates a reference for the active power component of the current. If Vdc drops, the PI controller injects more active power, maintaining capacitor charge, and if Vdc increases, the PI controller reduces SAPF power intake.

Fig. 19 shows the source voltages, the load currents, the source currents and the compensating current produced by SAPF with hysteresis control strategy and PI controller to correct the imbalance in the system. The load currents show a sharp increase while the source currents remain sinusoidal, and the source voltages are undisturbed. This control strategy decreases the THD of source current from 26.24% to 4.99% as shown in Fig. 20.

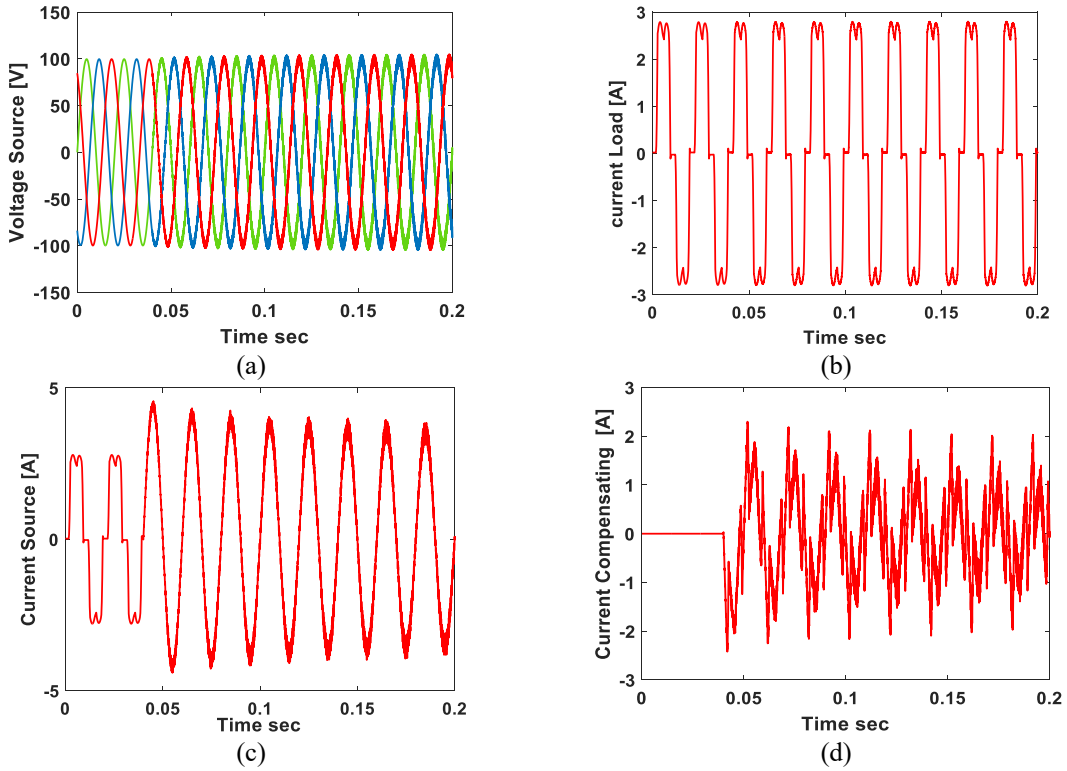

Fig. 19. Source voltages, Current load, Source current, Current Compensating

Despite the advantages of hysteresis control strategy: rapid dynamic response and good robustness with respect to parameter's changing like; inductance deviations, load changes and grid disturbances, it suffers from variable switching frequency that depends on DC-link voltage, hysteresis band width and load dynamics. It also suffers from high switching losses that reduce inverter efficiency.

8.3. Case III: The system with the Predictive Control Strategy for the SAPF and PI Controller

According to the SAPF's mathematical model of, the predictive control predicts the future compensating currents for each possible switching combination and selects the optimal switching state that leads to the minimum value of the objective function. This ensures that the future current follows the reference current with minimum error. Then, the VSI applies the chosen optimal switching state directly (no PWM). The PI controller is applied to adjust the DC-link capacitor voltage to stay constant.

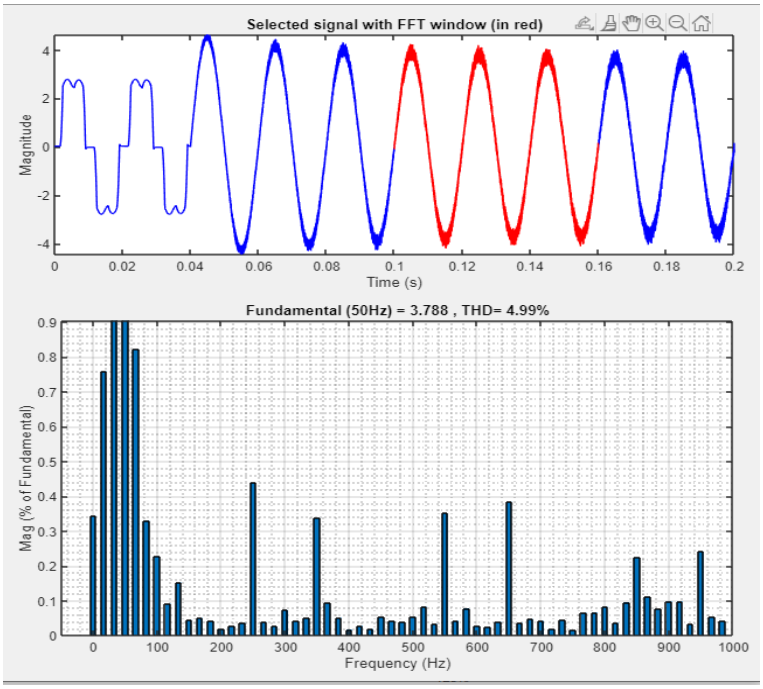

Fig. 20. Spectral analysis of the source current after commissioning of the SAPF

Fig. 21 shows the source currents, the load currents and the compensating current produced by SAPF with predictive control strategy and PI controller. It can be noticed that the results have been improved more than in hysteresis control strategy. This control strategy decreases the THD of source current from 4.99% to 3.35%, as shown in Fig. 22. The main advantages of predictive controller are: fixed switching frequency (unlike hysteresis controller) and direct control of inverter switches (no PWM required).

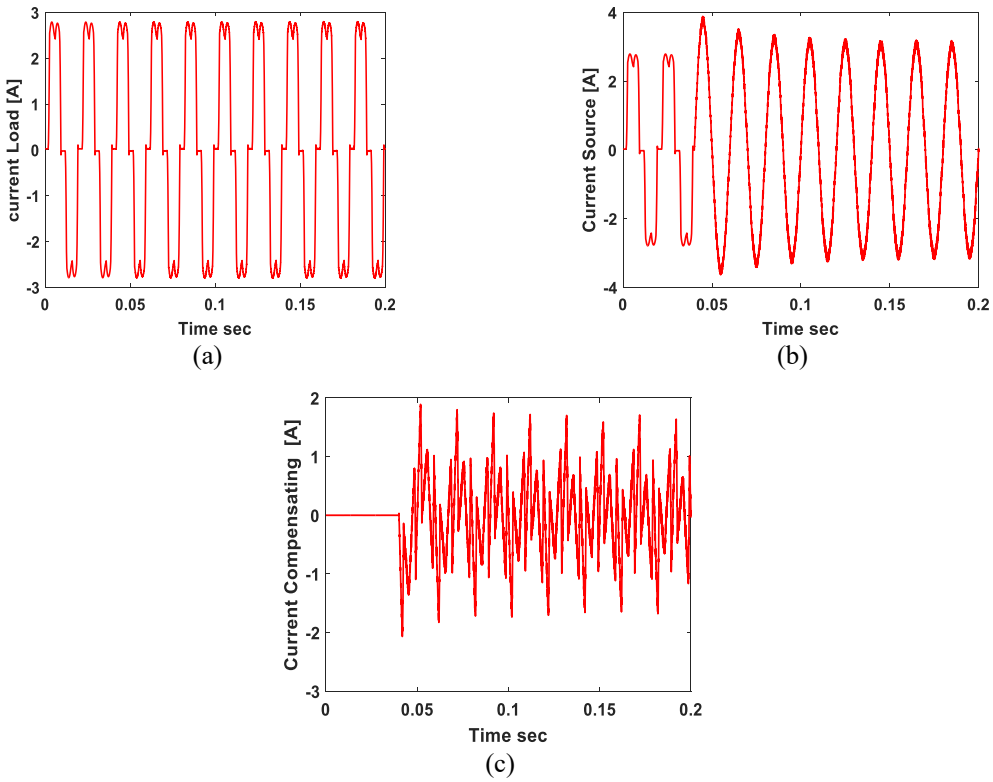

Fig. 21. Current load, Source current, Current Compensating

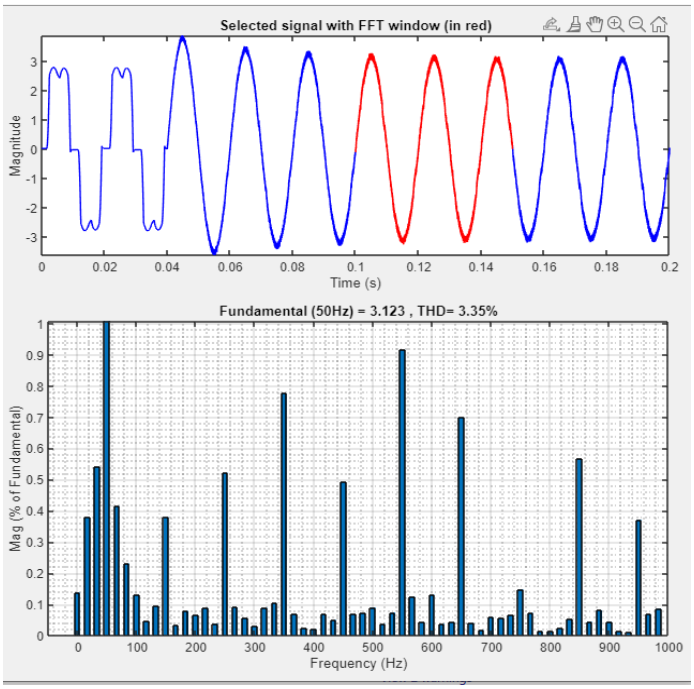

Fig. 22. Spectral analysis of the source current after commissioning of the SAPF (Predictive control)

8.4. Case IV: The System with the Predictive Control Strategy for the SAPF and (SCA-PI Controller)

The PI controller performance strongly depends on its parameters' values Kp and Ki. To improve the predictive control strategy and PI controller, we used the SCA theory with PI to tune the values of parameters Kp and Ki, which led to achieve an optimal regulation of the DC-link voltage. Fig. 23 shows that at t = 0.2 s (a) the load currents, (b) the source currents, (c) the compensating current. We noticed further improvement in the system, as seen in Fig. 24, where the THD has decreased compared to previous cases.

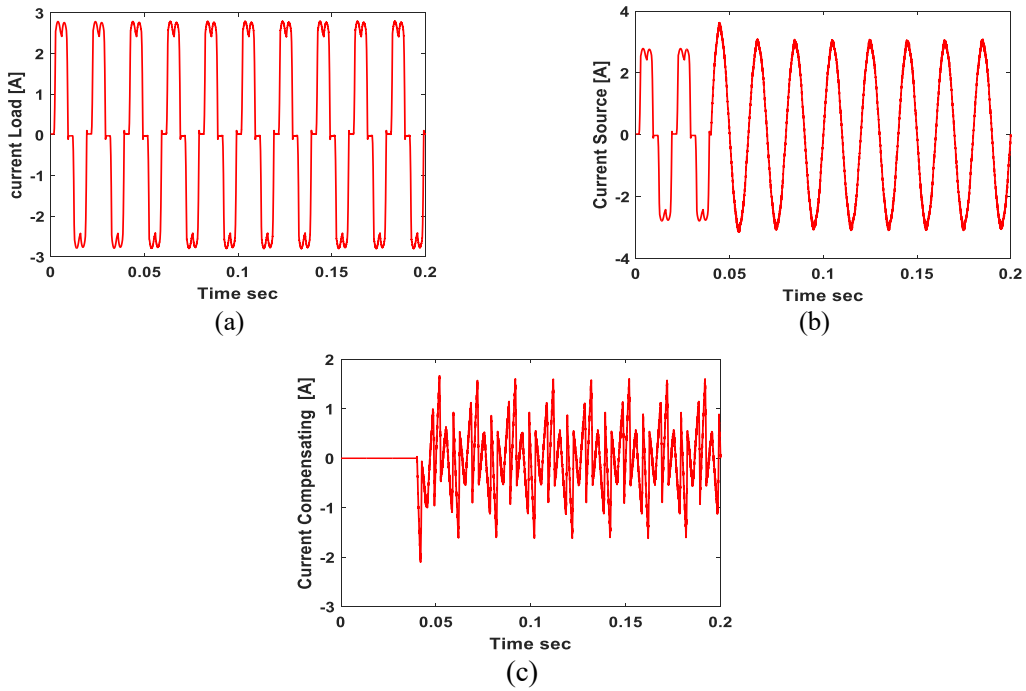

Fig. 23. Current load, Source current, Current Compensating

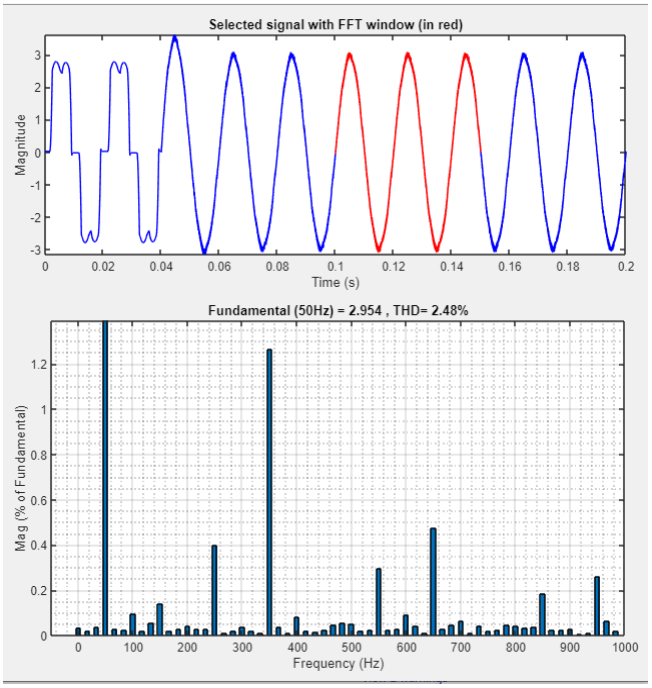

Fig. 24. Spectral analysis of the source current after commissioning of the SAPF (Predictive control_PI_SCA)

8.5. Case V: Comparison of DC-Link Voltage (PI and SCA-PI controller)

The effectiveness of the suggested control strategy MPCC-PI and MPCC-PI-SCA for SAPF have been tested and validated through MATLAB (Table 2). The DC link voltage with PI and SCA-PI controller are illustrated in Fig. 25 and Fig. 26. It asserts that the settling time and the rise of SCA-PI controller are better. Both controllers achieve good compensation, however, the SCA-PI controller provides the dominant execution. The DC link voltage obtained by using MPCC-PI-SCA shows good results comparing with MPCC-PI. It presents better settling time 0.0464 s and rise time 0.0650 s. The overshoot is very reduced.

Table 2. Comparison between (PI and SCA-PI controller)

	Rise time sec	Settling Time sec	Overshoot (%)	Kp	Ki
MPC-PI	0.0748	0.4429	7.7449	0.2	1.5
MPC-PI-SCA	0.0464	0.0650	0.00	2.2291	7

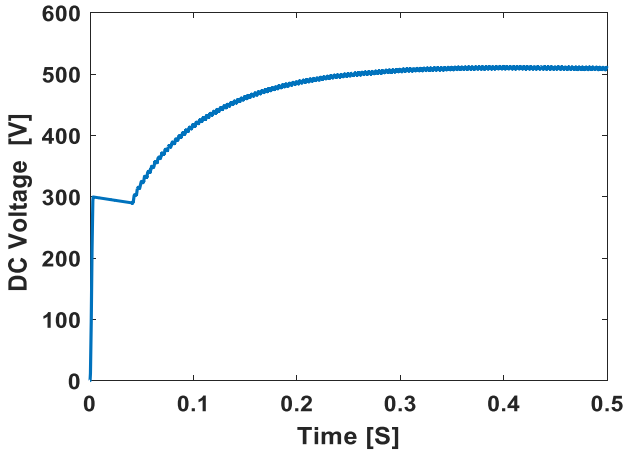

Fig. 25. DC-link voltage with PI controlled

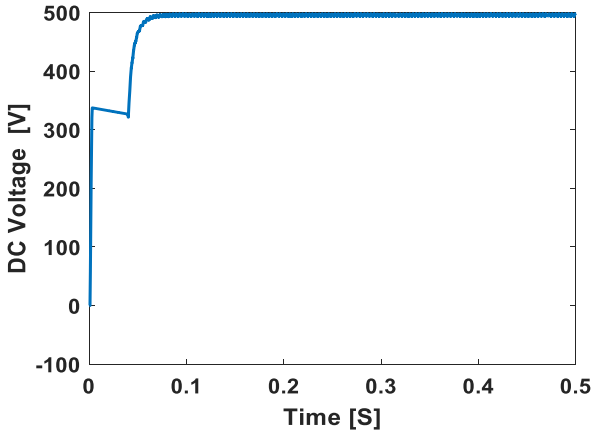

Fig. 26. DC-link voltage with SCA-PI controlled

9. Conclusions

This study addresses the issue of harmonic pollution in power systems, its origins, and its impact on the power grid. To address this issue, we enhanced the quality of the grid currents, hence reducing the system's THDi. A contemporary approach utilizing a shunt active filter controlled by model predictive control (MPCC) and energized by a wind energy generation. Based on the mathematical model of SAPF + grid + load, the proposed MPC predicts the future compensating currents and selects the optimal switching state by minimizing a cost function. Then, the chosen optimal switching state will be directly (no PWM) transmitted to the SAPF switches. To keep the DC-link voltage constant under all disturbance conditions, two controllers PI and SCA-PI have been used. SCA-PI controller is designed to handle real time, complex, non-linear problems. Met-heuristics algorithms such as SCA are well suited to globally explore space to find a good solution given a finite number of evaluations, whereas traditional algorithms often suffer from convergence issues and might trapped in local minima or have no guarantees of convergence. The SCA-PI controller allows to MPC to provide reliable and robust behavior against nonlinear load variations.

Author Contribution: All authors contributed equally to the main contributor to this paper. All authors read and approved the final paper.

Funding: This research received no external funding.

Conflicts of Interest: The authors declare no conflict of interest.

Appendix

Table 3. Wind power parameters

Components	Parameter Name	Rated Value
F	Stator frequency (Hz)	50 Hz
N	Synchronous speed (rev/min)	1800 rev/min
PS	Nominal stator three phase active power (rev/min)	2 MW
IS	Each phase nominal stator current (A)	1760 A
TEM	Nominal torque at generator (N.m)	12.732 N.m
P	Pole pair	2
RS	Stator resistance ($m\Omega$)	$2.6 \times m\Omega$
RR	Rotor resistance ($m\Omega$)	$2.9 \times m\Omega$
LM	Magnetic inductance (mH)	$2.5 \times m$H
N	Gearbox Ratio	100
R	Radio	44
ρ	Air density (Kg/m3)	1.225 Kg/m3

Table 4. Nonlinear load and Shunt active power filter parameters

Components	Parameter Name	Rated Value
R	Bridg PD3 three-phase	60 Ω
L	rectifier with R-L load	20 *m*H
R	Inductance filtering at	0.4 Ω
L	the input of the bridge PD3	3.55 *m*H
C	Storage capacity	35 µF
L	Coupling inductance	0.15 *m*H

References

[1] M. Awad, "A review of water electrolysis for green hydrogen generation considering PV/wind/hybrid/hydropower/geothermal/tidal and wave/biogas energy systems, economic analysis, and its application," *Alexandria Engineering Journal*, vol. 87, no. 18, pp. 213–239, 2024, https://doi.org/10.1016/j.aej.2023.12.032.

[2] M. M. Mahmoud, "Improved current control loops in wind side converter with the support of wild horse optimizer for enhancing the dynamic performance of PMSG-based wind generation system," *International Journal of Modelling and Simulation*, vol. 43, no. 6, pp. 952–966, 2023, https://doi.org/10.1080/02286203.2022.2139128.

[3] M. M. Mahmoud, M. K. Ratib, M. M. Aly, and A. M. M. Abdel-Rahim, "Wind-driven permanent magnet synchronous generators connected to a power grid: Existing perspective and future aspects," *Wind Engineering*, vol. 46, no. 1, pp. 189–199, 2022, https://doi.org/10.1177/0309524X211022728.

[4] O. Dahhani, A. El-Jouni, and I. Boumhidi, "Assessment and control of wind turbine by support vector machines," *Sustainable Energy Technologies and Assessments*, vol. 27, pp. 167–179, 2018, https://doi.org/10.1016/j.seta.2018.04.006.

[5] H. Alnami, S. A. E. M. Ardjoun, and M. M. Mahmoud, "Design, implementation, and experimental validation of a new low-cost sensorless wind turbine emulator: Applications for small-scale turbines," *Wind Engineering*, vol. 48, no. 4, pp. 565–579, 2024, https://doi.org/10.1177/0309524X231225776.

[6] M. Farbood, E. Taherian-Fard, M. Shasadeghi, A. Izadian, and T. Niknam, "Dynamics and control of a shared wind turbine drivetrain," *IEEE Transactions on Industry Applications*, vol. 54, no. 6, pp. 6394–6400, 2018, https://doi.org/10.1109/TIA.2018.2861758.

[7] M. M. Mahmoud, "Evaluation and comparison of different methods for improving fault ride-through capability in grid-tied permanent magnet synchronous wind generators," *International Transactions on Electrical Energy Systems*, vol. 2023, no. 1, pp. 1–22, 2023, https://doi.org/10.1155/2023/7717070.

[8] M. A. Bhayo, "An experimental hybrid control approach for wind turbine emulator," *IEEE Access*, vol. 11, pp. 58064–58077, 2023, https://doi.org/10.1109/ACCESS.2023.3283420.

[9] M. M. Mahmoud, M. M. Aly, H. S. Salama, and A. M. M. Abdel-Rahim, "A combination of an OTC-based MPPT and fuzzy logic current control for a wind-driven PMSG under variability of wind speed," *Energy Systems*, vol. 13, no. 4, pp. 1075–1098, 2022, https://doi.org/10.1007/s12667-021-00468-2.

[10] L. A. Soriano and J. D. J. Rubio, "Modeling and control of wind turbine," *Mathematical Problems in Engineering*, vol. 2013, no. 1, pp. 1–13, 2013, https://doi.org/10.1155/2013/982597.

[11] J. Liu, W. Yao, J. Wen, J. Fang, L. Jiang, H. He, and S. Cheng, "Impact of power grid strength and PLL parameters on stability of grid-connected DFIG wind farm," *IEEE Transactions on Sustainable Energy*, vol. 11, no. 1, pp. 545–557, 2020, https://doi.org/10.1109/TSTE.2019.2897596.

[12] J. Laafou, A. Ait Madi, A. Addaim, and A. Intidam, "Dynamic modeling and improved control of a grid-connected DFIG used in wind energy conversion systems," *Mathematical Problems in Engineering*, vol. 2020, no. 1, p. 1651648, 2020, https://doi.org/10.1155/2020/1651648.

[13] P. S. Kumar, R. P. S. Chandrasena, and K. V. S. M. Babu, "Design and implementation of wind turbine emulator using FPGA for stand-alone applications," *International Journal of Ambient Energy*, vol. 43, no. 1, pp. 2397–2409, 2022, https://doi.org/10.1080/01430750.2020.1736152.

[14] R. Sitharthan, T. Parthasarathy, S. S. Rani, and K. C. Ramya, "An improved radial basis function neural network control strategy-based maximum power point tracking controller for wind power generation system," *Transactions of the Institute of Measurement and Control*, vol. 41, no. 11, pp. 3158-3170, 2019, https://doi.org/10.1177/0142331218823858.

[15] R. Sitharthan, C. K. Sundarabalan, K. R. Devabalaji, S. K. Nataraj, and M. Karthikeyan, "Improved fault ride-through capability of DFIG wind turbines using customized dynamic voltage restorer," *Sustainable Cities and Society*, vol. 39, pp. 213–222, 2018, https://doi.org/10.1016/j.scs.2018.02.008.

[16] A. Hoseinpour and R. Ghazi, "Using of a three-phase four-switch inverter equipped with a variable index PWM to improve the power quality of a wind power plant," *International Journal of Industrial Electronics, Control and Optimization*, vol. 3, no. 3, pp. 213–222, 2020, https://doi.org/10.3390/pr12112586.

[17] S. Wang, J. Li, Z. Hou, Q. Meng, and M. Li, "Composite model-free adaptive predictive control for wind power generation based on full wind speed," *CSEE Journal of Power and Energy Systems*, vol. 8, no. 6, pp. 1659–1669, 2022, https://doi.org/10.17775/CSEEJPES.2019.02170.

[18] S. R. Mosayyebi, S. H. Shahalami, and H. Mojallali, "Fault ride-through capability improvement in a DFIG-based wind turbine using modified ADRC," *Protection and Control of Modern Power Systems*, vol. 7, no. 4, pp. 1–37, 2022, https://doi.org/10.1186/s41601-022-00272-9.

[19] J. D. Tan, C. C. W. Chang, and M. A. S. Bhuiyan, "Advancements of wind energy conversion systems for low-wind urban environments," *Energy Reports*, vol. 8, no. 11, pp. 3406–3414, 2022, https://doi.org/10.1016/j.egyr.2022.02.153.

[20] A. F. Tazay, A. M. A. Ibrahim, O. Noureldeen, and I. Hamdan, "Modeling, control, and performance evaluation of grid-tied hybrid PV/wind power generation system: Case study of Gabel El-Zeit Region, Egypt," *IEEE Access*, vol. 8, pp. 96528–96542, 2020, https://doi.org/10.1109/ACCESS.2020.2993919.

[21] B. Desalegn, D. Gebeyehu, and B. Tamrat, "Wind energy conversion technologies and engineering approaches to enhancing wind power generation," *Heliyon*, vol. 8, no. 11, p. e11263, 2022, https://doi.org/10.1016/j.heliyon.2022.e11263.

[22] S. Roga, S. Bardhan, Y. Kumar, and K. Dubey, "Recent technology and challenges of wind energy generation: A review," *Sustainable Energy Technologies and Assessments*, vol. 52, p. 102239, 2022, https://doi.org/10.1016/j.seta.2022.102239.

[23] P. K. Srivastava, A. N. Tiwari, and S. N. Singh, "Impacts of wind energy integration to the utility grid and grid codes: A review," *Recent Advances in Electrical and Electronic Engineering*, vol. 13, no. 4, pp. 446–469, 2020, https://doi.org/10.2174/2352096512666190709102957.

[24] L. Ge, C. Xu, H. Feng, H. Jiang, X. Li, and Y. Lu, "Study on isothermal pyrolysis and product characteristics of basic components of waste wind turbine blades," *Journal of Analytical and Applied Pyrolysis*, vol. 171, p. 105964, 2023, https://doi.org/10.1016/j.jaap.2023.105964.

[25] B. Diez-Canamero and J. M. F. Mendoza, "Circular economy performance and carbon footprint of wind turbine blade waste management alternatives," *Waste Management*, vol. 164, pp. 94–105, 2023, https://doi.org/10.1016/j.wasman.2023.03.041.

[26] J. Manso-Morato, N. Hurtado-Alonso, V. Revilla-Cuesta, and V. Ortega-Lopez, "Management of wind-turbine blade waste as high-content concrete addition: Mechanical performance evaluation and life cycle assessment," *Journal of Environmental Management*, vol. 373, p. 123995, 2025, https://doi.org/10.1016/j.jenvman.2024.123995.

[27] W. Zhang, H. Yu, B. Yin, A. Akbar, and K. M. Liew, "Sustainable transformation of end-of-life wind turbine blades: Advancing clean energy solutions in civil engineering through recycling and upcycling," *Journal of Cleaner Production*, vol. 426, p. 139184, 2023, https://doi.org/10.1016/j.jclepro.2023.139184.

[28] S. H. Mamanpush, H. Li, K. Englund, and A. T. Tabatabaei, "Recycled wind turbine blades as a feedstock for second generation composites," *Waste Management*, vol. 76, pp. 708–714, 2018, https://doi.org/10.1016/j.wasman.2018.02.050.

[29] S. Hosseini and M. Manthouri, "Type-2 adaptive fuzzy control approach applied to variable speed DFIG-based wind turbines with MPPT algorithm," *Iranian Journal of Fuzzy Systems*, vol. 19, no. 1, pp. 31–45, 2022, https://doi.org/10.22111/ijfs.2022.6549.

[30] K. A. Naik, C. P. Gupta, and E. Fernandez, "Design and implementation of interval type-2 fuzzy logic PI-based adaptive controller for DFIG-based wind energy system," *International Journal of Electrical Power and Energy Systems*, vol. 115, p. 105468, 2020, https://doi.org/10.1016/j.ijepes.2019.105468.

[31] A. Aggoune, F. Berrezzek, and K. Khelil, " Finite-Control-Set Model Predictive Control (FCS-MPC) and Fuzzy Self-Adaptive PI Controller (FSA-PIC) for wind turbine system based on DFIG," in *Proceedings of the 2nd International Conference on Nanotechnology for Environmental Protection and Clean Energy Production*, vol. 45, 2024, pp. 327–338, https://doi.org/10.1007/978-981-97-1916-7_34.

[32] A. V. Hemeyine, A. Abbou, N. Idjani, M. Mokhlis, and A. Bakouri, "Robust Takagi–Sugeno fuzzy models control for a variable speed wind turbine based on DFIG generator," *International Journal of Intelligent Engineering and Systems*, vol. 13, no. 3, pp. 90–100, 2020, https://doi.org/10.22266/ijies2020.0630.09.

[33] J. Hu, B. Wang, W. Wang, H. Tang, Y. Chi, and Q. Hu, "Small signal dynamics of DFIG-based wind turbines during riding through symmetrical faults in weak AC grid," *IEEE Transactions on Energy Conversion*, vol. 32, no. 2, pp. 720–730, 2017, https://doi.org/10.1109/TEC.2017.2655540.

[34] V. Le, X. Li, Y. Li, T. L. T. Dong, and C. Le, "An innovative control strategy to improve the fault ride-through capability of DFIGs based on wind energy conversion systems," *Energies*, vol. 9, no. 2, p. 69, 2016, https://doi.org/10.3390/en9020069.

[35] J. Mohammadi, S. Afsharnia, E. Ebrahimzadeh, and F. Blaabjerg, "An enhanced LVRT scheme for DFIG-based wind energy conversion systems under both balanced and unbalanced grid voltage sags," *Electric Power Components and Systems*, vol. 45, no. 11, pp. 1242–1252, 2017, https://doi.org/10.1080/15325008.2017.1333547.

[36] A. Bektache and B. Boukhezzar, "Nonlinear predictive control of a DFIG-based wind turbine for power capture optimization," *International Journal of Electrical Power and Energy Systems*, vol. 101, pp. 92–102, 2018, https://doi.org/10.1016/j.ijepes.2018.03.012.

[37] G. A. Parameswari and H. H. Sait, "A comprehensive review of fault ride-through capability of wind turbines with grid-connected doubly fed induction generator," *International Transactions on Electrical Energy Systems*, vol. 30, no. 8, p. e12395, 2020, https://doi.org/10.1002/2050-7038.12395.

[38] P. Verma and B. Dwivedi, "Comprehensive investigation on doubly fed induction generator wind farms at fault ride-through capabilities: Technical difficulties and improvisations," *Energy Sources, Part A: Recovery, Utilization, and Environmental Effects*, vol. 10, pp. 1–33, 2021, https://doi.org/10.1080/15567036.2020.1857476.

[39] S. R. Reddy, P. V. Prasad, and G. N. Srinivas, "Power quality enhancement using particle swarm optimization-based shunt active power filter," *International Journal of Mathematical Models and Methods in Applied Sciences*, vol. 16, pp. 134-139, 2022, https://doi.org/10.46300/9101.2022.16.22.

[40] Y. Aljarhizi, A. Nouaiti, E. Al Ibrahmi, C. Boutahiri, A. Hassoune, and A. Mesbahi, "Optimized wind turbine emulator based on an AC to DC motor generator set," *Engineering, Technology and Applied Science Research*, vol. 13, no. 2, pp. 10559–10564, 2023, https://doi.org/10.48084/etasr.5775.

[41] S. G. Reddy, S. Ganapathy, and M. Manikandan, "Three phase four switch inverter based DVR for power quality improvement with optimized CSA approach," *IEEE Access*, vol. 10, pp. 72263-72278, 2022, https://doi.org/10.1109/ACCESS.2022.3188629.

[42] D. K. Dash and P. K. Sadhu, "A review on the use of active power filter for grid-connected renewable energy conversion systems," *Processes*, vol. 11, no. 5, p. 1467, 2023, https://doi.org/10.3390/pr11051467.

[43] S. Biricik and H. Komurcugil, "Three-level hysteresis current control strategy for three-phase four-switch shunt active filters," *IET Power Electronics*, vol. 9, no. 8, pp. 1732–1740, 2016, https://doi.org/10.1049/iet-pel.2015.0764.

[44] N. Merayo, "PID controller based on a self-adaptive neural network to ensure QoS bandwidth requirements in passive optical networks," *Journal of Optical Communications and Networking*, vol. 9, no. 5, pp. 433–445, 2017, https://doi.org/10.1364/JOCN.9.000433.

[45] B. Wadawa, Y. Errami, A. Obbadi, S. Sahnoun, E. Chetouani, and M. Aoutoul, "Comparative application of the self-adaptive fuzzy-PI controller for a wind energy conversion system connected to the power grid and based on DFIG," *International Journal of Dynamics and Control*, vol. 10, no. 6, pp. 2151-2173, 2022, https://doi.org/10.1007/s40435-022-00952-2.

[46] S. Gupta and K. Deep, "A hybrid self-adaptive sine cosine algorithm with opposition-based learning," *Expert Systems with Applications*, vol. 119, pp. 210–230, 2019, https://doi.org/10.1016/j.eswa.2018.10.050.

[47] Y. Huo, Z. Chen, Q. Li, Q. Li, and M. Yin, "Machine Learning Based Model Predictive Control with Piecewise-Affine Approximation Structure for Maximizing Wind Energy Capture," *Journal of Modern Power Systems and Clean Energy*, vol. 13, no. 6, 2025, https://doi.org/10.35833/MPCE.2024.000886.

[48] H. K. E. Zine and K. Abed, "Smart current control of the wind energy conversion system based on permanent magnet synchronous generator using predictive and hysteresis model," *Electrical Engineering and Electromechanics*, no. 2, pp. 40–47, 2024, https://doi.org/10.20998/2074-272X.2024.2.06.

[49] H. Du, X. Hu, and C. Ma, "Dominant pole placement with modified PID controllers," *International Journal of Control, Automation and Systems*, vol. 17, pp. 2833–2838, 2019, https://doi.org/10.1007/s40534-021-00239-w.

[50] N. Hamouda, B. Babes, S. Kahla, C. Hamouda, and R. Uwe, "An optimized FO-PID controller and predictive current control of the APF connected AWPS for power quality improvement," *Przeglad Elektrotechniczny*, vol. 99, no. 5, pp. 102–107, 2023, https://doi.org/10.15199/48.2023.05.19.

[51] M. Khalili, M. A. Dashtaki, M. A. Nasab, H. R. Hanif, S. Padmanaban, B. Khan, and W. Meng, "Optimal instantaneous prediction of voltage instability due to transient faults in power networks taking into account the dynamic effect of generators," *Cogent Engineering*, vol. 9, no. 1, 2022, https://doi.org/10.1080/23311916.2022.2072568.

[52] U. Güvenç, A. Işik, T. Yiğit, and İ. Akkaya, "Performance analysis of biogeography-based optimization for automatic voltage regulator system," *Turkish Journal of Electrical Engineering and Computer Sciences*, vol. 24, no. 3, pp. 1150–1162, 2016, https://doi.org/10.3906/elk-1311-111.

[53] M. P. E. Rajamani, R. Rajesh, and M. W. Iruthayarajan, "A PID control scheme with enhanced non-dominated sorting genetic algorithm applied to a non-inverting buck–boost converter," *Sādhanā*, vol. 47, no. 4, p. 222, 2022, https://doi.org/10.1007/s12046-022-02012-z.

[54] M. H. Suid, M. A. Ahmad, S. Ahmad, M. F. M. Jusof, and Z. M. Tumari, "AVR system improvement: Fast and optimal tuning PID control using safe experimentation dynamics algorithm," in *Proceedings of the International Conference on System Science and Engineering*, 2024, pp. 1–5, https://doi.org/10.1109/ICSSE61472.2024.10608891.

[55] B. Hekimoğlu, "Sine cosine algorithm-based optimization for automatic voltage regulator system," *Transactions of the Institute of Measurement and Control*, vol. 41, no. 6, pp. 1761–1771, 2019, https://doi.org/10.1177/0142331218811453.

[56] R. R. Yujra and F. J. T. Vargas, "Performance and robustness of the response of an AVR with optimized PID using the sine cosine algorithm," *Acta Nova*, vol. 10, no. 3, pp. 303–317, 2022, http://www.scielo.org.bo/scielo.php?pid=S1683-07892022000100303&script=sci_abstract&tlng=en.

[57] A. B. Gabis, Y. Meraihi, S. Mirjalili, and A. Ramdane-Cherif, "A comprehensive survey of sine cosine algorithm: Variants and applications," *Artificial Intelligence Review*, vol. 54, no. 7, pp. 5469–5540, 2021, https://doi.org/10.1007/s10462-021-10026-y.

[58] M. Micev, M. Ćalasan, Z. M. Ali, H. M. Hasanien, and S. H. A. Aleem, "Optimal design of automatic voltage regulation controller using hybrid simulated annealing–manta ray foraging optimization algorithm," *Ain Shams Engineering Journal*, vol. 12, no. 1, pp. 641–657, 2021, https://doi.org/10.1016/j.asej.2020.07.010.

[59] X. Zhou, D. Li, L. Zhang, and Q. Duan, "Application of an adaptive PID controller enhanced by a differential evolution algorithm for precise control of dissolved oxygen in recirculating aquaculture systems," *Biosystems Engineering*, vol. 208, pp. 186–198, 2021, https://doi.org/10.1016/j.biosystemseng.2021.05.019.

[60] S. Abdel-Fatah, M. Ebeed, and S. Kamel, "Optimal reactive power dispatch using modified sine cosine algorithm," in *Proceedings of the 2019 International Conference on Innovative Trends in Computer Engineering*, 2019, pp. 510–514, https://doi.org/10.1109/ITCE.2019.8646460.